

Non-reflecting boundary conditions for atomistic, continuum and coupled atomistic/continuum simulations

Harold S. Park[‡], Eduard G. Karpov and Wing Kam Liu^{*,†}

Department of Mechanical Engineering, Northwestern University, 2145 Sheridan Road, Evanston, IL 60208-3111, U.S.A.

SUMMARY

We present a method to numerically calculate a non-reflecting boundary condition which is applicable to atomistic, continuum and coupled multiscale atomistic/continuum simulations. The method is based on the assumption that the forces near the domain boundary can be well represented as a linear function of the displacements, and utilizes standard Laplace and Fourier transform techniques to eliminate the unnecessary degrees of freedom. The eliminated degrees of freedom are accounted for in a time-history kernel that can be calculated for arbitrary crystal lattices and interatomic potentials, or regular finite element meshes using an automated numerical procedure. The new theoretical developments presented in this work allow the application of the method to non-nearest neighbour atomic interactions; it is also demonstrated that the identical procedure can be used for finite element and mesh-free simulations. We illustrate the effectiveness of the method on a one-dimensional model problem, and calculate the time-history kernel for FCC gold using the embedded atom method (EAM). Copyright © 2005 John Wiley & Sons, Ltd.

KEY WORDS: molecular dynamics; finite elements; non-reflecting boundary condition; multiple scales; generalized Langevin equation; coupling methods

1. INTRODUCTION

Molecular dynamics (MD) [1, 2] and finite elements (FE) [3, 4] are numerical techniques that are utilized to study the time-dependent response of atomistics and continua, respectively. Due to the constantly increasing computational power that is available to scientists and engineers, large-scale MD and FE simulations have become increasingly commonplace. However, in many MD and FE simulations of interest, such as fracture and material failure, much of the domain behaves in a manner which is readily modelled using elasticity theory. Only those atoms or

*Correspondence to: Wing Kam Liu, Department of Mechanical Engineering, Northwestern University, 2145 Sheridan Road, Evanston, IL 60208-3111, U.S.A.

†E-mail: w-liu@northwestern.edu

‡E-mail: hpark@alumni.northwestern.edu

Contract/grant sponsor: Publishing Arts Research Council; contract/grant number: 98-1846389

Received 25 August 2004

Revised 6 December 2004

Accepted 9 March 2005

Copyright © 2005 John Wiley & Sons, Ltd.

finite elements which directly surround the crack tip, shear band or failure mode of interest need to be directly simulated.

One approach to eliminate the unnecessary MD degrees of freedom stems from the work of Adelman and Doll [5]. In their work, the unwanted MD degrees of freedom in a one-dimensional harmonic chain were eliminated from the system; the effects of the eliminated atoms were included in a time-history-dependent force which was added to the boundary atoms. The time-history-dependent force consists of a matrix $\beta(t)$, termed the damping kernel matrix, multiplied by the boundary atom velocities. This force acts to dissipate energy into the eliminated degrees of freedom, and results in a non-reflecting MD boundary condition.

Due to the fact that analytical solutions for $\beta(t)$ are generally intractable in multiple dimensions, methods were developed to calculate the damping kernel matrix numerically. Examples include the work of Cai *et al.* [6] and Weinan and Huang [7]. Cai *et al.* calculated $\beta(t)$ by using multiple MD simulations of lattices which are somewhat larger than the domain of interest. The approach of E and Huang was different, as they performed an optimization problem to minimize the reflection coefficient at the MD boundary. Unfortunately, the size of the damping kernel matrix found using the approach of Cai *et al.* is related to the number of atoms on the MD boundary. In the E and Huang work, the geometry of the lattice must be explicitly modelled; this results in a new formulation for each different crystal lattice type.

In this work, we generalize the work of Wagner *et al.* [8], and Karpov *et al.* [9] by calculating the damping kernel $\beta(t)$, or equivalently its time derivative $\theta(t)$, known as the time-history kernel, for atomistic systems in which the atomic interactions extend beyond nearest neighbour. The method utilizes the inherent periodicity of crystalline lattices [10], and results in a damping kernel whose size is exactly that of the number of degrees of freedom in each unit cell. This work is motivated by the fact that most interatomic potentials that are used in MD simulations, such as the embedded atom method (EAM) [11], are inherently long ranged. Furthermore, it has been demonstrated in the MD literature that the behaviour observed in MD simulations can vary significantly depending on whether a nearest neighbour or non-nearest neighbour potential is used; see Reference [12] for an excellent example.

The previous works of Wagner *et al.* [8] and Karpov *et al.* [9] did consider longer-ranged interactions; however, the approach taken in that work was to extend the size of the unit cell to accommodate the longer-ranged interactions. Therefore, the size of the damping kernel matrix in that work increases as a function of the atomic interactions. In contrast, the unit cell in this work is always taken to be a single atom for monoatomic systems; the size of the damping kernel matrix does not increase as the interactions grow longer ranged.

While the method presented in this work has been previously used for generating non-reflecting MD boundary conditions, we show that, similar to the work of Kadowaki and Liu [13], the method is equally applicable for generating non-reflecting boundary conditions for FE or mesh-free simulations. The Kadowaki and Liu work utilized the method in the context of coupled multiscale FE/FE calculations; here, we demonstrate the approach on standard, single scale FE simulations. Analogous to utilizing a repetitive crystalline lattice, a regular finite element mesh is all that is required for the same theory to hold for continua.

The damping kernel matrix derived in this work is also applicable to multiple scale simulations that concurrently couple atomistics to continua. In particular, the recently developed bridging scale method of Wagner and Liu [14] and Park *et al.* [15–17] includes a boundary condition on the MD simulation involving the time-history kernel $\theta(t)$. Therefore, the time-history kernel derived in this work can be used without change in the bridging scale concurrent

method. Other approaches to eliminating spurious wave reflections for multiple scale simulations include the work of Xiao and Belytschko [18], who utilized spatial filtering at the MD/FEM interface to remove high-frequency wavelengths from the coupled simulation.

The layout of this paper is as follows. We first introduce the linearized equation of motion governing a repetitive crystalline lattice, then demonstrate how the unwanted MD degrees of freedom can be eliminated from the formulation. We compare the resulting displacement boundary condition to previously published works, and note the advantages of the proposed method. We then demonstrate the ease with which the identical theory can be utilized to generate the time-history kernel matrix for finite element simulations. A one-dimensional wave propagation example demonstrates the effectiveness of the method as a non-reflecting MD boundary condition, and the method is utilized to numerically calculate the time-history kernel for FCC gold using the EAM potential. Concluding remarks address the relative merits of the proposed approach.

2. NON-NEAREST NEIGHBOUR BOUNDARY CONDITION

The periodic crystal lattice we consider consists of spatially repeated unit cells which are replicated in three directions. Each repeated cell has n_a atoms, each of which can move in n_{SD} spatial directions. The total number of degrees of freedom, in each unit cell is then $n_{dof} = n_a \times n_{SD}$. Each unit cell can be labelled with three indices, l, m and n , indicating the position along axes in the direction of the three primitive vectors of the crystal structure. Figure 1 shows a two-dimensional hexagonal lattice lying in the y - z plane. Each atom represents a unit cell, and can be represented by (m, n) co-ordinates, with $l=0$ for this situation.

For the analysis to follow, it is not necessary to associate the (l, m, n) numbering with the elementary cells of the crystal. We utilize the more general concept of the unit cell, which can be both larger and smaller than the elementary cell. All that is required is that translations of the unit cell along l, m and n generate the entire lattice; it is not required that all triplets (l, m, n) correspond to physical locations of atoms. This is depicted in Figure 1, in which only unit cells with even $l + m + n$ are physically present.

This technique has certain advantages. Firstly, it allows the usage of orthogonal (l, m, n) numbering for the FCC structure in Figure 1, while keeping a monoatomic unit cell. The

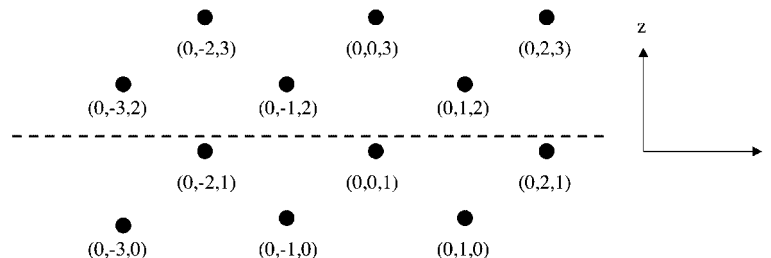


Figure 1. Repetitive two-dimensional hexagonal lattice structure numbered using unit cell nomenclature. The dashed line represents the boundary between the MD region to be simulated (bottom), and the MD region to be eliminated (top).

stiffness matrices \mathbf{K} , which are described later in this section, are symmetric with respect to the (l, m, n) numbering convention, and are of dimension 3×3 . Finally, this technique is useful for dealing with interfaces that are non-planar with the major crystallographic directions. Using the above approach, a monoatomic unit cell and the relevant translation vectors can always be found for a monoatomic lattice (for any crystallographic plane). We note, however, that the \mathbf{K} matrices may not always be symmetric depending on the nature of the non-planarity.

In MD, Newton's equations of motion are solved and updated for each atom in the system. For unit cell (l, m, n) , the equation of motion can be written as

$$\mathbf{M}\ddot{\mathbf{u}}_{l,m,n}(t) = \mathbf{f}_{l,m,n}^{\text{int}} + \mathbf{f}_{l,m,n}^{\text{ext}}(t) \quad (1)$$

where \mathbf{M} is a diagonal matrix of atomic masses, $\mathbf{f}_{l,m,n}^{\text{int}}(t)$ is the interatomic force, $\mathbf{f}_{l,m,n}^{\text{ext}}(t)$ is the external force and $\ddot{\mathbf{u}}_{l,m,n}$ is the acceleration, all of unit cell (l, m, n) . We linearize the interatomic force $\mathbf{f}_{l,m,n}^{\text{int}}(t)$ in the following manner for reasons to be detailed:

$$\mathbf{K}_{l-l',m-m',n-n'} = \left. \frac{\partial \mathbf{f}_{l,m,n}^{\text{int}}}{\partial \mathbf{u}_{l',m',n'}} \right|_{\mathbf{u}=0} \quad (2)$$

Using the linearized approximation for the interatomic force, the equation of motion (1) for unit cell (l, m, n) can be re-written as

$$\ddot{\mathbf{u}}_{l,m,n}(t) = \sum_{l'=l-2}^{l+2} \sum_{m'=m-2}^{m+2} \sum_{n'=n-2}^{n+2} \mathbf{M}^{-1} \mathbf{K}_{l-l',m-m',n-n'} \mathbf{u}_{l',m',n}(t) + \mathbf{M}^{-1} \mathbf{f}_{l,m,n}^{\text{ext}}(t) \quad (3)$$

where \mathbf{K} are the constant stiffness matrices relating the force on atom (l, m, n) to displacements \mathbf{u} of neighbouring atoms (l', m', n') . It is noteworthy that the summation over the stiffness coefficients extends from $n-2$ to $n+2$, indicating the longer-ranged interactions. We emphasize that even though the atomic interactions are long ranged, each atom in the lattice constitutes a unique unit cell.

By linearizing the interatomic force utilizing the constant stiffness matrices \mathbf{K} , we have developed in (3) a general expression by which the internal force on *every* unit cell in the lattice can be written as a combination of the same stiffness matrices \mathbf{K} , and the corresponding neighbouring atom displacements. The \mathbf{K} matrices are easily found in practice; one can simply perturb all neighbouring atoms of a unit cell while measuring the resulting force on the unit cell to calculate the \mathbf{K} matrices.

Equation (3) is valid for all the atoms in the system under consideration. However, as was stated in the Introduction, our goal is to limit the number of atoms in the MD computation. Therefore, the goal of the upcoming process will be to eliminate a large number of the atoms, while including their effects on the remaining lattice. As we will show, the assumption of linearity made above manifests itself *only* in the boundary condition due to the eliminated degrees of freedom; the remainder of the lattice interacts via non-linear interatomic forces. The material to follow assumes that we will eliminate all $n > 1$ atoms; the resulting MD boundary condition will then be dependent only on the $n = 0, 1$ atoms that remain.

The key point in extending previous works [8, 9] to incorporate long-ranged interactions is in recognizing that the motion of the $n = 0$ and $n = 1$ boundary atoms can be caused either by the motion of $n < 0$ atoms, or by an external force acting upon the boundary atoms. Thus, we

can enforce that the motion of $n=0$ and 1 boundary atoms is caused by an external constraint force, which acts only at $n=0$ and 1:

$$\mathbf{f}_{l,m,n}^{\text{ext}}(t) = \delta_{n,0} \mathbf{f}_{l,m,0}^{\text{ext}}(t) + \delta_{n,1} \mathbf{f}_{l,m,1}^{\text{ext}}(t) \quad (4)$$

For arbitrarily longer interactions, the constraint force must act upon all boundary planes of atoms whose neighbours include those atoms to be eliminated. We show now the detailed derivation for the case where a given unit cell interacts with all nearest and second nearest unit cells along directions orthogonal to the major crystallographic directions.

For this case, the virtual external force acts upon two planes of boundary atoms ($n=0,1$); this realization implies that the motion of the boundary atoms is caused entirely by the virtual external force. Taking a Laplace and discrete Fourier transform of (3) and solving for the resulting displacements $\hat{\mathbf{U}}$ gives

$$\hat{\mathbf{U}}(p,q,r,s) = \hat{\mathbf{G}}(p,q,r,s) (\mathbf{M}^{-1} \hat{\mathbf{F}}_0^{\text{ext}}(p,q,s) + e^{-i\tilde{r}} \mathbf{M}^{-1} \hat{\mathbf{F}}_1^{\text{ext}}(p,q,s) + s \hat{\mathbf{u}}(p,q,r,0) + \hat{\mathbf{u}}(p,q,r,0)) \quad (5)$$

where

$$\hat{\mathbf{G}}(p,q,r,s) = (s^2 \mathbf{I} - \hat{\mathbf{A}}(p,q,r))^{-1} \quad (6)$$

$$\tilde{r} = \frac{2\pi r}{L} \quad (7)$$

and p, q and r correspond to spatial indices l, m and n ; $\hat{\mathbf{A}}(p, q, r)$ is the discrete Fourier transform of $\mathbf{M}^{-1} \mathbf{K}_{l,m,n}$ and L is the number of unit cells in the x -direction. Basic properties of Laplace and Fourier transforms that are utilized throughout this work are given in the work of Wagner *et al.* [8]. We note that the combination of hatted and capital notation indicates both the Laplace and Fourier image of a function. The goal of this process is to eliminate the vectors $\hat{\mathbf{F}}_0^{\text{ext}}(p, q, s)$ and $\hat{\mathbf{F}}_1^{\text{ext}}(p, q, s)$. To do so, we perform an inverse discrete Fourier transform of (5) for r to give

$$\tilde{\mathbf{U}}_n(p, q, s) = \tilde{\mathbf{G}}_n(p, q, s) \mathbf{M}^{-1} \hat{\mathbf{F}}_0^{\text{ext}}(p, q, s) + \tilde{\mathbf{G}}_{n-1}(p, q, s) \mathbf{M}^{-1} \hat{\mathbf{F}}_1^{\text{ext}}(p, q, s) + \tilde{\mathbf{R}}_n(p, q, s) \quad (8)$$

where

$$\tilde{\mathbf{R}}_n(p, q, s) = s \sum_{n'=-N/2+1}^{N/2} \tilde{\mathbf{G}}_{n-n'}(p, q, s) \tilde{\mathbf{u}}_{n'}(p, q, 0) + \sum_{n'=-N/2+1}^{N/2} \tilde{\mathbf{G}}_{n-n'} \dot{\tilde{\mathbf{u}}}_{n'}(p, q, 0) \quad (9)$$

and N is the number of unit cells in the z -direction. We note that in deriving (8), the expression

$$\mathcal{F}(g_{n+h}) = \hat{g}(r) e^{ihr} \quad (10)$$

known as the shift theorem was utilized. We next write (8) for $n=0, 1, 2, 3$ to give

$$\tilde{\mathbf{U}}_0(p, q, s) = \tilde{\mathbf{G}}_0(p, q, s) \mathbf{M}^{-1} \hat{\mathbf{F}}_0^{\text{ext}}(p, q, s) + \tilde{\mathbf{G}}_{-1}(p, q, s) \mathbf{M}^{-1} \hat{\mathbf{F}}_1^{\text{ext}}(p, q, s) + \tilde{\mathbf{R}}_0(p, q, s) \quad (11)$$

$$\tilde{\mathbf{U}}_1(p, q, s) = \tilde{\mathbf{G}}_1(p, q, s) \mathbf{M}^{-1} \hat{\mathbf{F}}_0^{\text{ext}}(p, q, s) + \tilde{\mathbf{G}}_0(p, q, s) \mathbf{M}^{-1} \hat{\mathbf{F}}_1^{\text{ext}}(p, q, s) + \tilde{\mathbf{R}}_1(p, q, s) \quad (12)$$

$$\tilde{\mathbf{U}}_2(p, q, s) = \tilde{\mathbf{G}}_2(p, q, s)\mathbf{M}^{-1}\hat{\mathbf{F}}_0^{\text{ext}}(p, q, s) + \tilde{\mathbf{G}}_1(p, q, s)\mathbf{M}^{-1}\hat{\mathbf{F}}_1^{\text{ext}}(p, q, s) + \tilde{\mathbf{R}}_2(p, q, s) \quad (13)$$

$$\tilde{\mathbf{U}}_3(p, q, s) = \tilde{\mathbf{G}}_3(p, q, s)\mathbf{M}^{-1}\hat{\mathbf{F}}_0^{\text{ext}}(p, q, s) + \tilde{\mathbf{G}}_2(p, q, s)\mathbf{M}^{-1}\hat{\mathbf{F}}_1^{\text{ext}}(p, q, s) + \tilde{\mathbf{R}}_3(p, q, s) \quad (14)$$

Here, the tilde notation implies mixed Fourier images, which depend on both the original and transform values. We can now use the above equations to make two relations. First, we will relate the virtual forces to the displacements of atoms 0 and 1. We use (11) and (12) to give

$$\begin{pmatrix} \hat{\mathbf{F}}_0^{\text{ext}}(p, q, s) \\ \hat{\mathbf{F}}_1^{\text{ext}}(p, q, s) \end{pmatrix} = \begin{pmatrix} \tilde{\mathbf{G}}_0(p, q, s) & \tilde{\mathbf{G}}_{-1}(p, q, s) \\ \tilde{\mathbf{G}}_1(p, q, s) & \tilde{\mathbf{G}}_0(p, q, s) \end{pmatrix}^{-1} \mathbf{M} \begin{pmatrix} \tilde{\mathbf{U}}_0(p, q, s) - \tilde{\mathbf{R}}_0(p, q, s) \\ \tilde{\mathbf{U}}_1(p, q, s) - \tilde{\mathbf{R}}_1(p, q, s) \end{pmatrix} \quad (15)$$

We use (13) and (14) to express the displacements of atoms 2 and 3 in terms of the virtual external forces as

$$\begin{pmatrix} \tilde{\mathbf{U}}_2(p, q, s) \\ \tilde{\mathbf{U}}_3(p, q, s) \end{pmatrix} = \mathbf{M}^{-1} \begin{pmatrix} \tilde{\mathbf{G}}_2(p, q, s) & \tilde{\mathbf{G}}_1(p, q, s) \\ \tilde{\mathbf{G}}_3(p, q, s) & \tilde{\mathbf{G}}_2(p, q, s) \end{pmatrix} \begin{pmatrix} \hat{\mathbf{F}}_0^{\text{ext}}(p, q, s) \\ \hat{\mathbf{F}}_1^{\text{ext}}(p, q, s) \end{pmatrix} + \begin{pmatrix} \tilde{\mathbf{R}}_2(p, q, s) \\ \tilde{\mathbf{R}}_3(p, q, s) \end{pmatrix} \quad (16)$$

We substitute (15) into (16) to obtain

$$\begin{pmatrix} \tilde{\mathbf{U}}_2(p, q, s) \\ \tilde{\mathbf{U}}_3(p, q, s) \end{pmatrix} = \tilde{\mathbf{Q}}(p, q, s) \begin{pmatrix} \tilde{\mathbf{U}}_0(p, q, s) - \tilde{\mathbf{R}}_0(p, q, s) \\ \tilde{\mathbf{U}}_1(p, q, s) - \tilde{\mathbf{R}}_1(p, q, s) \end{pmatrix} + \begin{pmatrix} \tilde{\mathbf{R}}_2(p, q, s) \\ \tilde{\mathbf{R}}_3(p, q, s) \end{pmatrix} \quad (17)$$

where

$$\tilde{\mathbf{Q}}(p, q, s) = \begin{pmatrix} \tilde{\mathbf{G}}_2(p, q, s) & \tilde{\mathbf{G}}_1(p, q, s) \\ \tilde{\mathbf{G}}_3(p, q, s) & \tilde{\mathbf{G}}_2(p, q, s) \end{pmatrix} \begin{pmatrix} \tilde{\mathbf{G}}_0(p, q, s) & \tilde{\mathbf{G}}_{-1}(p, q, s) \\ \tilde{\mathbf{G}}_1(p, q, s) & \tilde{\mathbf{G}}_0(p, q, s) \end{pmatrix}^{-1} \quad (18)$$

By inverting the Fourier and Laplace transforms in (18), we can analytically obtain the desired displacement boundary conditions acting upon the reduced MD domain to be

$$\begin{pmatrix} \mathbf{u}_{l,m,2}(t) \\ \mathbf{u}_{l,m,3}(t) \end{pmatrix} = \sum_{l'=-L/2+1}^{L/2} \sum_{m'=-M/2+1}^{M/2} \int_0^t \boldsymbol{\theta}_{l-l',m-m'}(t-\tau) \begin{pmatrix} \mathbf{u}_{l,m,0}(\tau) - \mathbf{R}_{l,m,0}(\tau) \\ \mathbf{u}_{l,m,1}(\tau) - \mathbf{R}_{l,m,1}(\tau) \end{pmatrix} + \begin{pmatrix} \mathbf{R}_{l,m,2}(t) \\ \mathbf{R}_{l,m,3}(t) \end{pmatrix} \quad (19)$$

where

$$\boldsymbol{\theta}_{l-l',m-m'}(t-\tau) = \begin{pmatrix} \boldsymbol{\theta}_{l-l',m-m'}^{(11)}(t-\tau) & \boldsymbol{\theta}_{l-l',m-m'}^{(12)}(t-\tau) \\ \boldsymbol{\theta}_{l-l',m-m'}^{(21)}(t-\tau) & \boldsymbol{\theta}_{l-l',m-m'}^{(22)}(t-\tau) \end{pmatrix} \quad (20)$$

$$\boldsymbol{\theta}_{l,m}(t) = \mathcal{L}_{s \rightarrow t}^{-1} \mathcal{F}_{p,q \rightarrow l,m}^{-1}(\tilde{\mathbf{Q}}(p, q, s)) \quad (21)$$

In general, the random component of the displacement can be written as

$$\begin{aligned} \mathbf{R}_{l,m,n}(t) = & \sum_{l'=-L/2+1}^{L/2} \sum_{m'=-M/2+1}^{M/2} \sum_{n'=-N/2+1}^{N/2} \dot{\mathbf{g}}_{l-l',m-m',n-n'}(t) \mathbf{u}_{l',m',n'}(0) \\ & + \sum_{l'=-L/2+1}^{L/2} \sum_{m'=-M/2+1}^{M/2} \sum_{n'=-N/2+1}^{N/2} \mathbf{g}_{l-l',m-m',n-n'}(t) \dot{\mathbf{u}}_{l',m',n'}(0) \end{aligned} \quad (22)$$

where

$$\mathbf{g}_{l,m,n}(t) = \mathcal{L}^{-1}(\mathbf{G}_{l,m,n}(s)) \quad (23)$$

$$\dot{\mathbf{g}}_{l,m,n}(t) = \mathcal{L}^{-1}\{s\mathbf{G}_{l,m,n}(s)\} \quad (24)$$

In (22), L , M and N are the total number of unit cells in the x -, y - and z -directions, respectively. Because the analytic solution of (19) requires the displacements of all $n=0$ and $n=1$ plane atoms, we truncate the summation to a critical number of atomic planes l_c and m_c . The resulting MD equation of motion for the remaining atoms and the boundary conditions can be written as

$$\mathbf{M}\ddot{\mathbf{u}}(t) = \mathbf{f}(t) \quad (25)$$

where

$$\mathbf{f}(t) = -\frac{\partial\Phi(\mathbf{r})}{\partial\mathbf{r}} \quad (26)$$

subject to displacement boundary conditions

$$\begin{aligned} \begin{pmatrix} \mathbf{u}_{l,m,2}(t) \\ \mathbf{u}_{l,m,3}(t) \end{pmatrix} = & \sum_{l'=l-l_c}^{l+l_c} \sum_{m'=m-m_c}^{m+m_c} \int_0^t \boldsymbol{\theta}_{l-l',m-m'}(t-\tau) d\tau \\ & \times \begin{pmatrix} \mathbf{u}_{l,m,0}(\tau) - \mathbf{R}_{l,m,0}(\tau) \\ \mathbf{u}_{l,m,1}(\tau) - \mathbf{R}_{l,m,1}(\tau) \end{pmatrix} + \begin{pmatrix} \mathbf{R}_{l,m,2}(t) \\ \mathbf{R}_{l,m,3}(t) \end{pmatrix} \end{aligned} \quad (27)$$

where

$$\mathbf{R}_{l,m,n}(t) = \left(\sum_{l',m',n'} \dot{\mathbf{g}}_{l-l',m-m',n-n'}(t) \dot{\mathbf{u}}_{l',m',n'}(0) + \mathbf{g}_{l-l',m-m',n-n'}(t) \dot{\mathbf{u}}_{l',m',n'}(0) \right) \quad (28)$$

Thus, the interatomic force \mathbf{f} for the remaining MD lattice can be calculated using any non-linear potential energy function $\Phi(\mathbf{r})$. This is possible because the linearity of the MD system (i.e. the constant \mathbf{K} assumption) is *only* required in the elimination of the $n > 1$ atoms, and is entirely contained within the time-history kernels $\boldsymbol{\theta}(t)$.

2.1. Comments on resulting formulation

- The increase in atomic interaction distance results in a corresponding increase in the number of time-history kernel matrices $\boldsymbol{\theta}(t)$; for the case shown above, there are four instances of $\boldsymbol{\theta}(t)$. This due to the fact that if longer-ranged interactions are used, more planes of atoms away from the boundary require boundary conditions.
- In practice, the $n=2$ and 3 displacements correspond to ghost atom displacements, which are necessary such that the crystal does not relax due to spurious free-surface effects. Because the motion of ghost atoms is not determined by integrating the MD equations of motion, their motion must be prescribed differently. In this formulation, the ghost atom $n=2$ and 3 displacements, which provide displacement boundary conditions, are functions of the known $n=0$ and 1 boundary atom displacements.
- The underlying formulation has not changed; the major difference is that the summation over the stiffness matrices in (3) has been increased to account for the longer-ranged interactions.
- Analogous to the fact that the eliminated MD degrees of freedom are accounted for in $\boldsymbol{\theta}(t)$, the thermal effects of the eliminated MD degrees of freedom are accounted for in the random components of the displacement $\mathbf{R}_{l,m,n}(t)$; this term was first derived by Adelman and Doll [5]. Thus, the random component of the displacement is thermally motivated, and balances the energy that is dissipated out of the MD region by the time-history kernel $\boldsymbol{\theta}(t)$. Taking the random portion of the displacements to be zero, as is done in this work, implies that the eliminated MD degrees of freedom are at 0K. However, this does not place any restrictions on the temperature of the MD region which is kept for simulation. The current authors have also developed a method to efficiently derive the random displacements $\mathbf{R}_{l,m,n}(t)$ based on the Gibbs canonical distribution; this will be presented in a future publication [19].
- The size of the $\boldsymbol{\theta}(t)$ matrices in (27) has not changed; each $\boldsymbol{\theta}(t)$ matrix still has the size of the minimum number of degrees of freedom in each unit cell. For a monoatomic unit cell in one dimension, $\boldsymbol{\theta}(t)$ is a scalar; in two dimensions, $\boldsymbol{\theta}(t)$ is a 2×2 matrix, in three dimensions, $\boldsymbol{\theta}(t)$ is a 3×3 matrix.

2.2. Advantages of displacement formulation

Previous incarnations of non-reflecting MD boundary conditions [5–7] have utilized a force formulation in which the effects of the eliminated degrees of freedom acts as an external force on the remaining boundary atoms. The displacement formulation presented here may be advantageous to the force formulation for the following reasons:

- The displacement $\boldsymbol{\theta}(t)$ requires less computational effort than the $\boldsymbol{\theta}(t)$ that is necessary for the force formulation; this is because the force formulation requires an additional convolution with the stiffnesses \mathbf{K} after having calculated the displacements in (17).
- As can be seen from (18), the time-history kernel $\boldsymbol{\theta}(t)$ is independent of scaling parameters of an interatomic potential. Thus, $\boldsymbol{\theta}(t)$ can be thought of as an inherent quantity for a given lattice structure.
- Using the displacement formulation results in an easier implementation in MD codes; once the displacement boundary conditions in (27) are found, the MD force subroutine can then continue without change. If the force formulation is used, then modifications to the external force vector in the MD equations of motion are required.

2.3. Algorithm for numerical implementation

We now detail the programming flowchart for the numerical calculation of the time-history kernel $\boldsymbol{\theta}(t)$. The flowchart mimics that given in Reference [8]. The algorithm assumes there are L, M and N unit cells in the x -, y - and z -directions, respectively. Our numerical experiments indicate that using values of around $L = M = N = 32$ are sufficient to mimic the response of a very large crystal. The limit of $L = M = N = 32$ was determined by analysing the calculated values for $\boldsymbol{\theta}(t)$ for smaller values of L, M and N ; once the larger values for L, M and N had been reached, the numerically calculated values for $\boldsymbol{\theta}(t)$ had not changed from using smaller values of L, M and N , hence it was determined that a converged value for $\boldsymbol{\theta}(t)$ had been reached. We note that due to the finiteness of the parameters and the usage of numerical Fourier transforms, the time-history kernels $\boldsymbol{\theta}(t)$ should be truncated at some value of time t to avoid the artificial reflections off periodic boundaries.

Before initiating the procedure, it is assumed that the stiffness matrices \mathbf{K} are known for a given crystal structure, for interaction ranges $|l| \leq \mu$, $|m| \leq \nu$ and $|n| \leq \rho$. Once these are known, the algorithm proceeds as

(i) For each (p, q, r) , form $\hat{\mathbf{A}}(p, q, r)$:

$$\hat{\mathbf{A}}(p, q, r) = \sum_{l=-\lambda}^{\lambda} \sum_{m=-\mu}^{\mu} \sum_{n=-\nu}^{\nu} \mathbf{M}^{-1} \mathbf{K}_{l,m,n} e^{-i2\pi(lp/L + mq/M + nr/N)} \quad (29)$$

(ii) For each (p, q, r, s) , compute $\hat{\mathbf{G}}(p, q, r, s)$:

$$\hat{\mathbf{G}}(p, q, r, s) = (s^2 \mathbf{I} - \hat{\mathbf{A}}(p, q, r))^{-1} \quad (30)$$

(iii) For each (p, q, s) , invert the DFT in the z -direction at $n = -1, 0, 1, 2, 3$:

$$\tilde{\mathbf{G}}_n(p, q, s) = \frac{1}{N} \sum_{r=-(N/2)+1}^{N/2} \hat{\mathbf{G}}(p, q, r, s) e^{2\pi i r n / N}, \quad n = -1, 0, 1, 2, 3 \quad (31)$$

(iv) For each (p, q, s) , compute $\tilde{\mathbf{Q}}(p, q, s)$:

$$\tilde{\mathbf{Q}}(p, q, s) = \begin{pmatrix} \tilde{\mathbf{G}}_2(p, q, s) & \tilde{\mathbf{G}}_1(p, q, s) \\ \tilde{\mathbf{G}}_3(p, q, s) & \tilde{\mathbf{G}}_2(p, q, s) \end{pmatrix} \begin{pmatrix} \tilde{\mathbf{G}}_0(p, q, s) & \tilde{\mathbf{G}}_{-1}(p, q, s) \\ \tilde{\mathbf{G}}_1(p, q, s) & \tilde{\mathbf{G}}_0(p, q, s) \end{pmatrix}^{-1} \quad (32)$$

(v) For each l, m and s compute the IFT of $\tilde{\mathbf{Q}}(p, q, s)$:

$$\mathbf{Q}_{l,m}(s) = \frac{1}{LM} \sum_{p=-(L/2)+1}^{L/2} \sum_{q=-(M/2)+1}^{M/2} \tilde{\mathbf{Q}}(p, q, s) e^{2\pi i(mq/M + lp/L)} \quad (33)$$

(vi) For each l and m , compute the ILT to get the time-history kernel:

$$\boldsymbol{\theta}_{m,n}(t) = \mathcal{L}^{-1} \{ \mathbf{Q}_{l,m}(s) \} \quad (34)$$

Now that the algorithm has been fully laid out, we make further comments:

- The most expensive part of the algorithm are steps (i–ii), in which the inverse of the matrix involving $\hat{\mathbf{A}}(p, q, r)$ must be calculated for all (p, q, r, s) .
- The algorithm can easily be adapted to calculate the time-history kernel on different faces of a crystal. For example, to calculate the kernel for the y -directions, the DFT would be inverted in the y -direction at $n=0$ and 1 in step (iii), with the corresponding changes made in future steps.
- The IFT in step (v) need not be calculated for all l and m . Specifically, the short-ranged nature of the interatomic potential can be utilized here to truncate l and m after only a few terms.
- The inverse Laplace transform (ILT) needed in step (vi) can be efficiently and accurately calculated using the method of Weeks [20].
- The major differences in this algorithm and that presented by Wagner *et al.* [8] are as follows. Firstly, the summations over the \mathbf{K} matrices in each direction in step (i) will be larger. Secondly, $\tilde{\mathbf{Q}}(p, q, s)$ in step (iv) is a block matrix of dimension $n \times n$, where n is the number of unit cells along directions orthogonal to the major crystallographic directions. Both of these differences are due to the increased range of the interatomic potential. In the work of Wagner *et al.*, n was chosen to be 1. In this work, for the derivation and numerical examples presented, we adopt $n=2$.
- One advantage between this work and that presented by Wagner *et al.* [8] can be seen in Equation (30). In this work, due to the compact size of the stiffness matrices \mathbf{K} , a smaller matrix must be inverted for all (p, q, r, s) to obtain $\hat{\mathbf{G}}(p, q, r, s)$. In the earlier work [8], because the stiffness matrices \mathbf{K} increase in size along with the interaction range of the potential, a larger matrix must be inverted for non-nearest neighbour potentials for all (p, q, r, s) to obtain $\hat{\mathbf{G}}(p, q, r, s)$.

3. APPLICATION TO FINITE ELEMENT METHODS

3.1. One-dimensional linear finite elements

We first illustrate the applicability of the method presented in this work to finite elements utilizing the simplest case, that of linear finite elements. We note that linear finite elements do not require the long-ranged formulation shown in this work, but we present the illustration due to the simplicity and familiarity of one-dimensional linear finite elements. The semi-discrete equations of motion for a three-node, two-element system can be written as

$$\begin{pmatrix} m\ddot{u}_{I-1} \\ m\ddot{u}_I \\ m\ddot{u}_{I+1} \end{pmatrix} = \begin{pmatrix} f_{I-1}^{\text{ext}} \\ f_I^{\text{ext}} \\ f_{I+1}^{\text{ext}} \end{pmatrix} - \begin{pmatrix} 2K & -K & 0 \\ -K & 2K & -K \\ 0 & -K & 2K \end{pmatrix} \begin{pmatrix} u_{I-1} \\ u_I \\ u_{I+1} \end{pmatrix} \quad (35)$$

where m is the lumped mass at each node and $K = AE/l_e$, where A is the cross-sectional area, E is the Young's modulus and l_e is the length of each element. We note that the stiffness coefficients K in (35) correspond exactly to those MD stiffness coefficients which are required in (2). We assume that node I constitutes the boundary of the FE domain, implying that we

will eliminate all nodes $\geq I + 1$. The repetitive structure of the internal force is visible in the middle equation in (35), which shows that the internal force acting on *any* node I in the FE system can be written as

$$f_I^{\text{int}} = Ku_{I-1} - 2Ku_I + Ku_{I+1} \quad (36)$$

The tie between atomistics and finite elements and thus the ability of the proposed method to work for both systems is seen in (36), which exactly corresponds to the linearized force acting upon an atom in a one-dimensional chain interacting with its nearest neighbours. In fact, it is simply a convenient coincidence that the nodal internal force for a linear FE system coincides with the interatomic force for a nearest-neighbour MD potential; the crucial element which allows applicability of the method to both systems is that the force on *every* node or atom is a repetitive function of the same stiffness coefficients. Thus, the method which was originally developed for MD is directly applicable to FE.

Therefore, the same method which was presented in References [8, 9, 13] and is being extended in the present work can be utilized to calculate the time-history kernel $\theta(t)$ for this FE system, with the only difference being that the atomic spring constant k is replaced by AE/l_e for the continuum. As was shown in Reference [8], the time-history kernel can be found analytically for this one-dimensional system to be

$$\theta(t) = \frac{2}{t} J_2(2\omega t) \quad (37)$$

where for the continuum system the frequency ω is defined as $\omega = (\sqrt{E/\rho})/l_e$, ρ is the density of the material and J_2 indicates a second-order Bessel function. The time-history kernel given in (37) relates the displacement [8, 9, 13] of node $I + 1$ to boundary node I as

$$u_{I+1} = \int_0^t \theta(t - \tau) u_I(\tau) d\tau \quad (38)$$

Thus, the internal force for boundary node I in (36) can be written in final form as

$$f_I^{\text{int}} = Ku_{I-1} - 2Ku_I + K \int_0^t \theta(t - \tau) u_I(\tau) d\tau \quad (39)$$

This equation accounts for all eliminated nodes $\geq I + 1$ in the time-history kernel $\theta(t)$, and results in a non-reflecting FE boundary condition.

3.2. Mesh-free methods in one-dimension

Considering all atomic interactions within second nearest unit cells in directions orthogonal to the major crystallographic directions leads, in one dimension, to a stiffness matrix whose repetitive bandwidth has five elements. In finite elements, a stiffness matrix of this bandwidth can be obtained using mesh-free shape functions [21, 22]. In this section, we will demonstrate that the procedure given above holds identically for mesh-free methods.

For mesh-free methods, the values of the components of the stiffness matrix will change depending on the support size, the order of polynomial completeness desired, and the method utilised. Assuming that the factors previously mentioned lead to a stiffness matrix with a

bandwidth of five elements, we write the internal force for a five node mesh-free system as

$$\begin{pmatrix} f_{I-2}^{\text{int}} \\ f_{I-1}^{\text{int}} \\ f_I^{\text{int}} \\ f_{I+1}^{\text{int}} \\ f_{I+2}^{\text{int}} \end{pmatrix} = \begin{pmatrix} K_0 & K_{-1} & K_{-2} & 0 & 0 \\ K_1 & K_0 & K_{-1} & K_{-2} & 0 \\ K_2 & K_1 & K_0 & K_{-1} & K_{-2} \\ 0 & K_2 & K_1 & K_0 & K_{-1} \\ 0 & 0 & K_2 & K_1 & K_0 \end{pmatrix} \begin{pmatrix} u_{I-2} \\ u_{I-1} \\ u_I \\ u_{I+1} \\ u_{I+2} \end{pmatrix} \quad (40)$$

The repetitive portion of the internal force on arbitrary node I is seen in the middle equation of (40), and can be written as

$$f_I^{\text{int}} = K_2 u_{I-2} + K_1 u_{I-1} + K_0 u_I + K_{-1} u_{I+1} + K_{-2} u_{I+2} \quad (41)$$

We assume that all nodes $\geq I + 1$ are to be eliminated, which corresponds to displacement degrees of freedom u_{I+1} and u_{I+2} in (40). However, the known solution for those eliminated degrees of freedom was found in (27). Substituting (27) into (40) gives the non-reflecting boundary condition for nodes I and $I - 1$:

$$\begin{aligned} f_{I-1}^{\text{int}} &= K_2 u_{I-3} + K_1 u_{I-2} + K_0 u_{I-1} + K_{-1} u_I \\ &+ K_{-2} \left(\int_0^t \boldsymbol{\theta}^{(11)}(t-\tau) u_{I-1}(\tau) \, d\tau + \int_0^t \boldsymbol{\theta}^{(12)}(t-\tau) u_I(\tau) \, d\tau \right) \end{aligned} \quad (42)$$

$$\begin{aligned} f_I^{\text{int}} &= K_2 u_{I-2} + K_1 u_{I-1} + K_0 u_I \\ &+ K_{-1} \left(\int_0^t \boldsymbol{\theta}^{(11)}(t-\tau) u_{I-1}(\tau) \, d\tau + \int_0^t \boldsymbol{\theta}^{(12)}(t-\tau) u_I(\tau) \, d\tau \right) \\ &+ K_{-2} \left(\int_0^t \boldsymbol{\theta}^{(21)}(t-\tau) u_{I-1}(\tau) \, d\tau + \int_0^t \boldsymbol{\theta}^{(22)}(t-\tau) u_I(\tau) \, d\tau \right) \end{aligned} \quad (43)$$

We note that no special treatment is needed at the boundary due to the mesh-free shape functions because we have assumed that the elimination of the FE nodal degrees of freedom has occurred away from the original boundary of the FE domain.

4. NUMERICAL EXAMPLES

4.1. One-dimensional wave propagation

We verify the accuracy of our formulation by running a one-dimensional MD wave propagation example using a harmonic potential of the form

$$\Phi(r) = \frac{1}{2} k(r - r_0)^2 \quad (44)$$

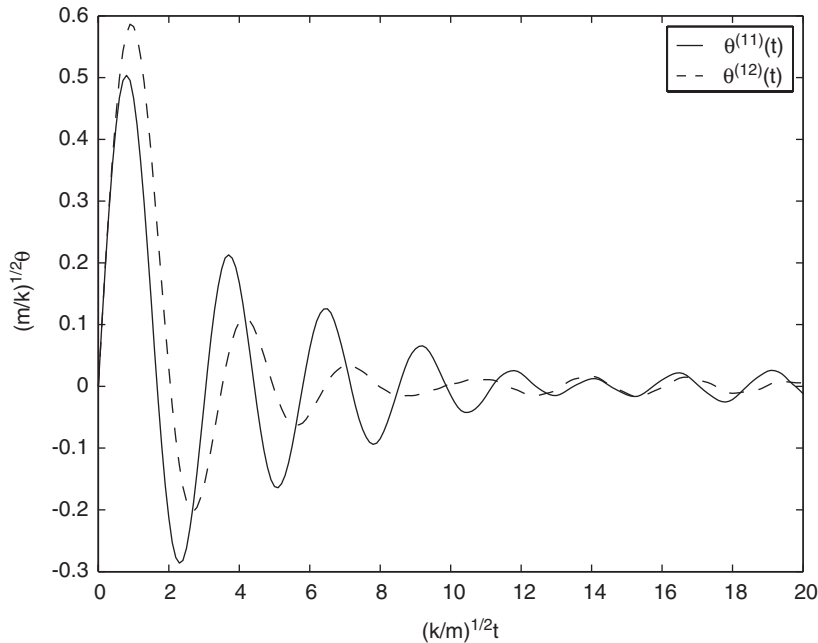


Figure 2. Plots of time-history kernels $\theta^{(11)}(t)$ and $\theta^{(12)}(t)$ truncated at normalized time $t=20$ for a harmonic potential.

where r is the pairwise deformed bond length, r_0 is the equilibrium bond length and k is the spring constant. Using this harmonic potential, the stiffness coefficients k that are necessary to calculate the time-history kernels $\theta(t)$ assuming atomic interactions are truncated after second nearest unit cells along directions orthogonal to the major crystallographic directions are

$$K_{-2} = K_2 = K_{-1} = K_1 = k \quad (45)$$

$$K_0 = -4k \quad (46)$$

Using these stiffness coefficients, we numerically calculate the time-history kernels $\theta(t)$ in (27) using the procedure detailed in Section 2.3. Using the values $k=1$ and atomic masses $m=1$, the values of $\theta(t)$ can be seen in Figures 2 and 3.

We note that the values of $\theta(t)$ resulting from the longer-ranged interactions behave similarly as those for the nearest neighbour case [8, 9], particularly in that all kernels decay quickly as functions of time. Another important feature which can be gleaned by visual analysis is that all components of $\theta(t)$ appear to be of similar magnitude; therefore, it is expected that ignoring these components in numerical analysis will lead to large inaccuracies and retention of energy in the MD region.

The MD simulation contained 226 atoms between $x = -0.375$ and $x = 0.375$ for an interatomic spacing of $h_a = \frac{2}{3}r_0$, where $r_0 = 0.005$. The spring constant k and atomic masses m were chosen to be unity, and 1000 MD time steps with a time step $\Delta t = 0.2$ were chosen for

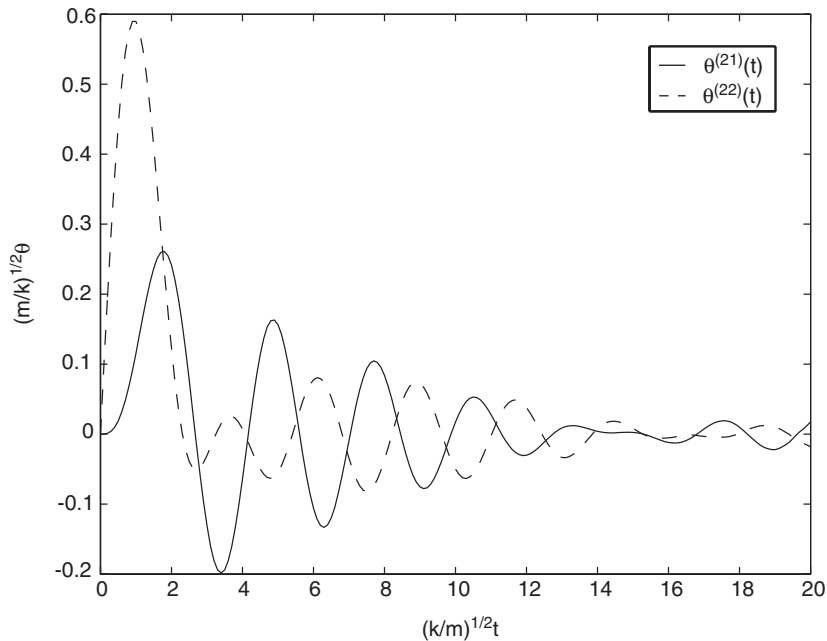


Figure 3. Plots of time-history kernels $\theta^{(21)}$ and $\theta^{(22)}(t)$ truncated at normalized time $t=20$ for a harmonic potential.

the simulation. A benchmark full MD simulation consisting of 1001 atoms between $x = -1.5$ and 1.5 with the same interatomic spacing $h_a = \frac{2}{3} r_0$ was run for verification purposes. The initial displacements given to the MD region were in the form of a Gaussian wave with a combination of high and low frequencies similar to References [14, 15], and is shown in Figure 4.

To complete the problem description, atomic interactions are truncated after second nearest unit cells.

For the 226-atom MD simulations, the ghost atom displacements $u_2(t)$ and $u_3(t)$ were calculated using (27) and the $\theta(t)$ shown in Figures 2 and 3. We measure the quality of the MD boundary condition by monitoring the total energy of the MD region during the course of the simulation. The energy history of the MD region is depicted in Figure 5. As can be seen, if the interface atom displacements are calculated correctly, more than 99 per cent of the initial MD energy is correctly dissipated away. Furthermore, the energy leaves the MD region at the same time as in the full MD simulation, verifying the accuracy of the reduced MD simulation.

A final comment concerns the time scales for which it is necessary to calculate $\theta(t)$. In observing the time duration of the MD simulation in Figure 5 compared to the time for which $\theta(t)$ is calculated in Figures 2 and 3, it is clear that $\theta(t)$ is calculated for a normalized time of 40, while the simulation is carried out to a normalized time of 200. The simulation was also carried out with the time-history kernels $\theta(t)$ in Figures 2 and 3 calculated for a normalized time of 120. As can be seen by the energy transfer comparison in Figure 5, little gain in accuracy is achieved by calculating the time-history kernels for lengthy portions of the simulation; this is due to the rapidly decaying property of the time-history kernels $\theta(t)$.

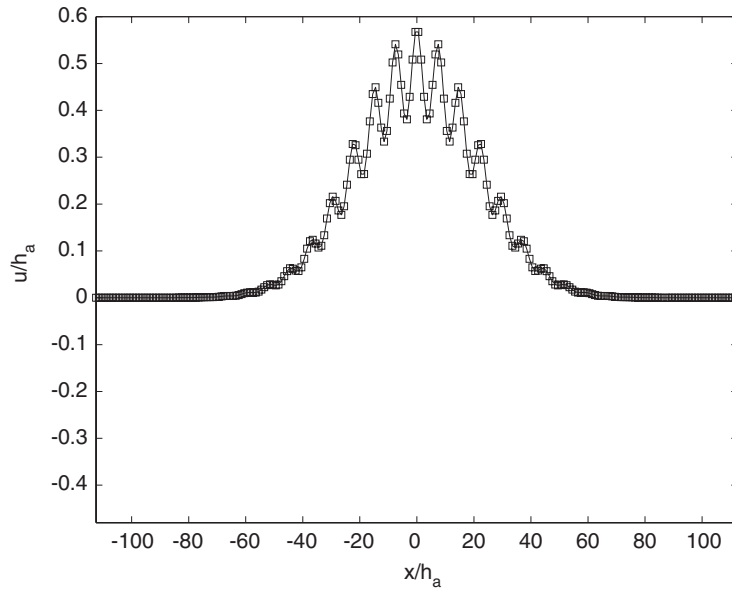


Figure 4. Initial MD displacements for one-dimensional wave propagation problem.

A spatial truncation can also be employed for computational efficiency, and is represented by the truncated summation over l_c and m_c in (27). The combined spatial and temporal truncations were utilized by Park *et al.* [16, 23] in two- and three-dimensional multiple scale analyses of dynamic fracture; it was found that taking l_c and $m_c = 0$ or 1 was sufficient for numerical simulations.

4.2. Time-history kernels for FCC gold

In this section, we present calculations of the time-history kernel $\boldsymbol{\theta}(t)$ for FCC gold using the embedded atom method (EAM) [11]. The parameters used for FCC gold are identical to those found in the work of Foiles *et al.* [24], which has been implemented in the Sandia simulation code Tahoe [25]. The EAM gold potential considers interactions with second nearest unit cells in each crystallographic direction, identical to the formulation presented in this paper, which means that 43 \mathbf{K} matrices need to be found in order to calculate $\boldsymbol{\theta}(t)$ correctly. Those \mathbf{K} matrices were found by systematically perturbing all neighbours of a unit cell, and are given in the Appendix.

Recalling that each sub-matrix of $\boldsymbol{\theta}(t)$ is itself a 3×3 matrix, as in (20), we show only selected components of $\boldsymbol{\theta}^{(22)}$. In particular, noting that $\boldsymbol{\theta}^{(22)}$ can be written as

$$\boldsymbol{\theta}^{(22)}(t) = \begin{pmatrix} \boldsymbol{\theta}_{11}^{(22)}(t) & \boldsymbol{\theta}_{12}^{(22)}(t) & \boldsymbol{\theta}_{13}^{(22)}(t) \\ \boldsymbol{\theta}_{21}^{(22)}(t) & \boldsymbol{\theta}_{22}^{(22)}(t) & \boldsymbol{\theta}_{23}^{(22)}(t) \\ \boldsymbol{\theta}_{31}^{(22)}(t) & \boldsymbol{\theta}_{32}^{(22)}(t) & \boldsymbol{\theta}_{33}^{(22)}(t) \end{pmatrix} \quad (47)$$

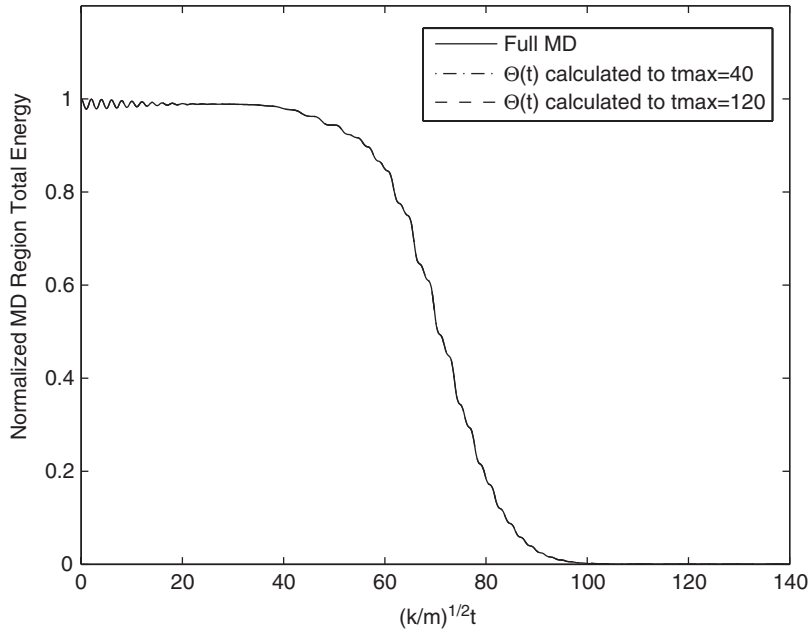


Figure 5. Comparison of energy transferred from MD region between full MD simulation and two reduced MD simulations utilizing $\theta(t)$ calculated for different amounts of time.

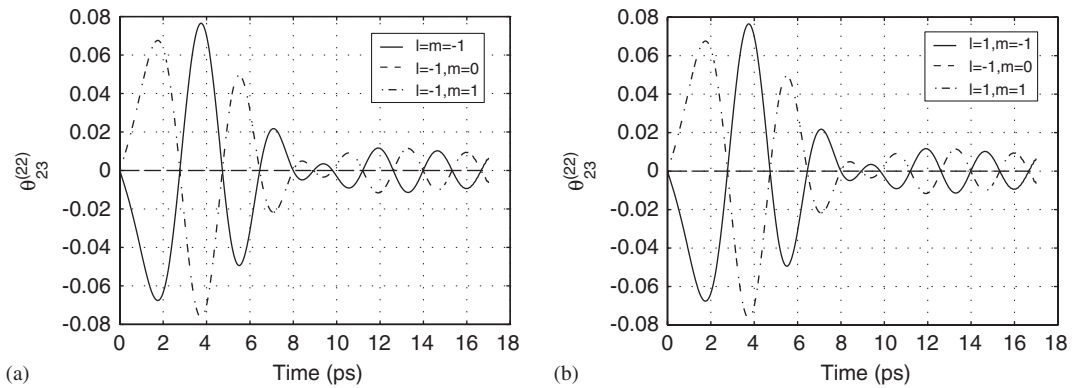


Figure 6. (a) $\theta_{23}^{(22)}(t)$ for $l = -1, m = -1, 0, 1$; and (b) $\theta_{23}^{(22)}(t)$ for $l = 1, m = -1, 0, 1$.

We show only the specific components $\theta_{23}^{(22)}(t)$ and $\theta_{33}^{(22)}$. These are shown in Figures 6–8. To aid in the visualization, we introduce Figure 9, which depicts all neighbours for atom $(0, 0, 0)$ within the x - y plane.

One interesting feature present in all the figures is that all time-history kernels have a value of zero for those lattice sites at which a neighbouring atom is not present. These zero

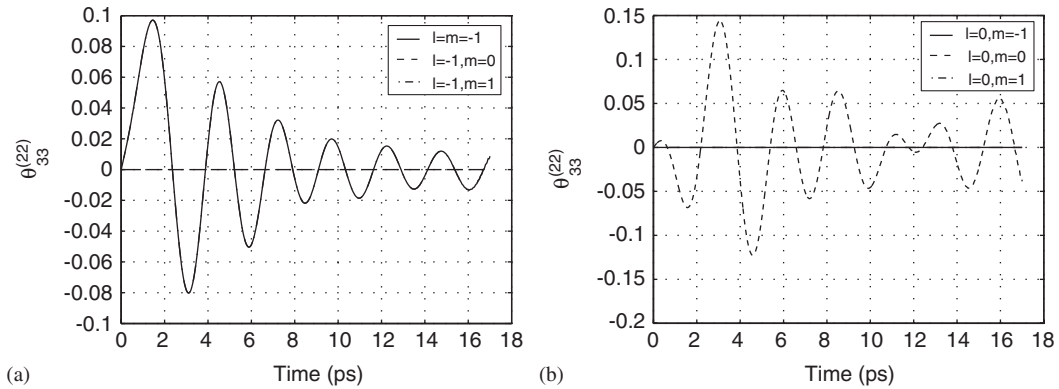


Figure 7. (a) $\theta_{33}^{(22)}(t)$ for $l = -1, m = -1, 0, 1$; and (b) $\theta_{33}^{(22)}(t)$ for $l = 0, m = -1, 0, 1$.

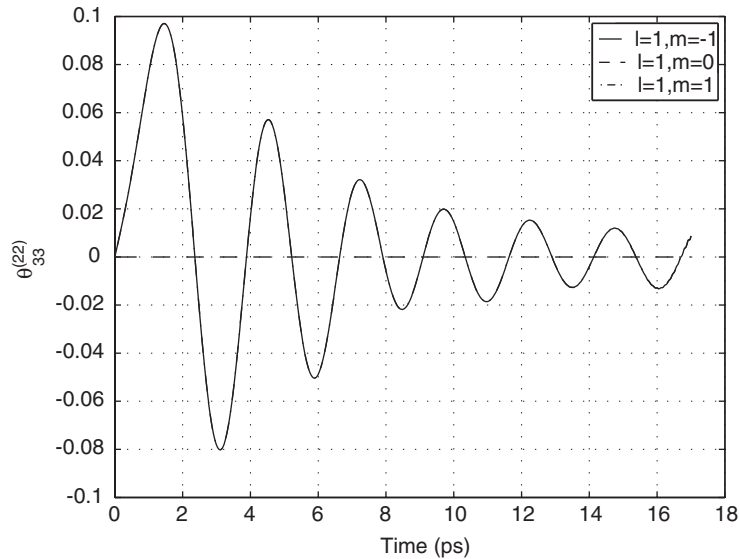


Figure 8. $\theta_{33}^{(22)}(t)$ for $l = 1; m = -1, 0, 1$.

atom positions correspond to lattice sites $(\pm 1, 0, 0)$ and $(0, \pm 1, 0)$, and can be seen to be true by direction comparison with Figure 9. In Figures 6–8, all values of $\theta(t)$ are zero for those positions at which a neighbouring atom is not present, and represents a check on the correctness of the method. This fact also illustrates how the geometry of the lattice need not be explicitly modelled in this approach.

Another interesting feature is in the symmetries exhibited by the time-history kernels. Due to the symmetry of an FCC crystal, one would expect to correspondingly see some sort of

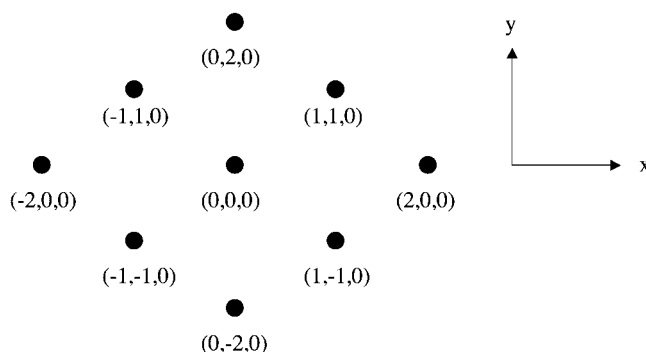


Figure 9. All neighbours of atom $(0, 0, 0)$ within the x - y plane.

symmetry in the crystal response, and that is indeed observed. Specifically, those pairs of atoms with one spatial co-ordinate as the negative of the other, such as $l = -1, m = 1$ and $l = -1, m = -1$ either have the same time-history values, as in Figures 7 and 8, or are related by a negative, as in Figures 6(a) and (b).

Finally, most values of the kernels tend to decay quickly over relatively short periods of time. This again leads to gains in computational efficiency by reducing the storage requirements necessary for the boundary atom displacement histories.

5. CONCLUSIONS

We have presented a method to calculate a non-reflecting boundary condition which is valid for molecular dynamics, finite elements, and coupled multiscale atomistic/continuum simulations. The assumptions underlying the method include a linearized representation of the dynamics near the domain boundary, and a spatially repetitive atomic lattice or finite element mesh. This approach offers clear advantages as compared to previous methods, namely the compact size of the time-history kernel, the fact that the geometry of the lattice or finite element mesh need not be explicitly modelled, and the fact that the time-history kernel can be calculated using an automated numerical procedure. Due to the fact that the basic unit cell for monoatomic systems is always a single atom, the size of the time-history kernel matrix $\theta(t)$ is constant, and does not grow as a function of the atomic interaction distance.

The major theoretical improvement as compared to previous works [8, 9, 13] is that long-ranged atomic interactions or non-local finite element and mesh-free methods can be used with the approach presented in this work. This extension is necessary as the atomistic phenomena observed during fracture, void growth and nucleation, and other interesting phenomena varies dramatically depending on whether nearest neighbour or non-nearest-neighbour interactions are considered [12].

Practically speaking, the method presented allows the accurate calculation of the MD ghost atom displacements (27), which are necessary such that the reduced MD region does not spuriously relax due to surface effects. Because the method modifies only the ghost atom

displacements, no change is necessary in the MD internal force subroutine once the ghost atom positions have been calculated. For FE simulations, the method gives the displacements of the eliminated nodes near the boundary; these displacements can then simply be multiplied by the correct entry of the FE stiffness matrix to give the required force acting upon the reduced FE system.

The method presented was validated on a simple one-dimensional MD wave propagation example. As was clearly shown, the MD boundary condition presented allowed the clean dissipation of both long and short wavelengths out of the MD region, allowing the reduced MD lattice to behave as if part of a much larger structure. Furthermore, when compared to a full, benchmark MD simulation, the reduced MD simulation utilizing the time-history kernels $\theta(t)$ were shown to allow energy to leave the MD region at the same time as the full MD simulation. Computational efficiency is gained due to the rapid decay of the time-history kernels $\theta(t)$; the kernels can be truncated after short time periods with negligible loss in accuracy.

Due to the assumptions made in calculating the time-history kernel, the method presented herein does not apply to certain situations. For example, due to the assumption of a crystalline and repetitive lattice, the method is not valid for fluids or gases. Furthermore, the method will lose accuracy at non-planar boundaries such as corners, or will be insufficient in the case where defects, such as dislocations approach the boundary. However, many MD and FE problems of interest involve physical phenomena which are relatively localized in space; this observation has motivated the development of multiscale methods, in which the atomistic region of the problem is assumed to exist only in a small portion of the problem domain.

We close with three final comments. Firstly, the time-history kernels derived in this work can be used directly without change in the multiple scale method developed by Wagner and Liu [14], and extended by Park *et al.* [16,23]. Secondly, Karpov *et al.* [19] have developed a method to apply the stochastic thermal component $\mathbf{R}(t)$ of the ghost atom displacements (27); development in this direction is critical such that the reduced MD domain can operate at finite temperatures. Finally, while the numerical examples in this work were limited to one dimension, the central idea behind this method has been applied in multiple dimensions by Park *et al.* [16,23], and Kadowaki and Liu [13].

APPENDIX A: EAM \mathbf{K} -MATRICES FOR 3D FCC GOLD

In this section, we show the three-dimensional \mathbf{K} -matrices for a third shell EAM potential for FCC Gold. For a third shell FCC potential, each atom has 43 neighbouring atoms; each of the 43 atoms in this test lattice were perturbed such that the resulting force on cell $(0,0,0)$ resulting from the perturbation could be determined. We now write the \mathbf{K} -matrices which are given in units of $\text{eV}/\text{\AA}^2$:

$$\mathbf{K}_{0,0,0} = \begin{pmatrix} -4.415218 & 0 & 0 \\ 0 & -4.415218 & 0 \\ 0 & 0 & -4.415218 \end{pmatrix} \quad (\text{A1})$$

$$\mathbf{K}_{0,0,2} = \mathbf{K}_{0,0,-2}^T = \begin{pmatrix} -0.06714876 & 0 & 0 \\ 0 & -0.06714876 & 0 \\ 0 & 0 & 0.0371758 \end{pmatrix} \quad (\text{A2})$$

$$\mathbf{K}_{2,0,0} = \mathbf{K}_{-2,0,0} = \begin{pmatrix} 0.03717614 & 0 & 0 \\ 0 & -0.06714876 & 0 \\ 0 & 0 & -0.06714876 \end{pmatrix} \quad (\text{A3})$$

$$\mathbf{K}_{0,2,0} = \mathbf{K}_{0,-2,0}^T = \begin{pmatrix} -0.06714876 & 0 & 0 \\ 0 & -0.03717614 & 0 \\ 0 & 0 & -0.067114876 \end{pmatrix} \quad (\text{A4})$$

$$\mathbf{K}_{-1,0,1} = \mathbf{K}_{1,0,-1}^T = \begin{pmatrix} -0.5980576 & 0 & -0.71029 \\ 0 & -0.1736703 & 0 \\ -0.710314 & 0 & 0.5980418 \end{pmatrix} \quad (\text{A5})$$

$$\mathbf{K}_{-1,0,-1} = \mathbf{K}_{1,0,1}^T = \begin{pmatrix} 0.5980579 & 0 & 0.710314 \\ 0 & -0.1736703 & 0 \\ 0.710314 & 0 & 0.5980579 \end{pmatrix} \quad (\text{A6})$$

$$\mathbf{K}_{0,-1,1} = \mathbf{K}_{0,1,-1}^T = \begin{pmatrix} -0.1736703 & 0 & 0 \\ 0 & 0.5980579 & -0.71029 \\ 0 & -0.710314 & 0.5980418 \end{pmatrix} \quad (\text{A7})$$

$$\mathbf{K}_{0,-1,-1} = \mathbf{K}_{0,1,1}^T = \begin{pmatrix} -0.1736703 & 0 & 0 \\ 0 & 0.5980579 & 0.710314 \\ 0 & 0.710314 & 0.5980579 \end{pmatrix} \quad (\text{A8})$$

$$\mathbf{K}_{1,1,0} = \mathbf{K}_{-1,-1,0} = \begin{pmatrix} 0.5980418 & 0.71029 & 0 \\ 0.71029 & 0.5980418 & 0 \\ 0 & 0 & -0.1736703 \end{pmatrix} \quad (\text{A9})$$

$$\mathbf{K}_{1,-1,0} = \mathbf{K}_{-1,1,0}^T = \begin{pmatrix} 0.5980418 & -0.710314 & 0 \\ -0.71029 & 0.5980418 & 0 \\ 0 & 0 & -0.1736703 \end{pmatrix} \quad (\text{A10})$$

$$\mathbf{K}_{1,1,2} = \mathbf{K}_{-1,-1,-2} = \begin{pmatrix} -0.003171257 & 0.03711209 & 0.04007788 \\ 0.03711209 & -0.003171257 & 0.04007788 \\ 0.04029503 & 0.04029503 & 0.07131029 \end{pmatrix} \quad (\text{A11})$$

$$\mathbf{K}_{1,1,-2} = \mathbf{K}_{-1,-1,2} = \begin{pmatrix} -0.003171257 & 0.03711209 & -0.04007788 \\ 0.03711209 & -0.003171257 & -0.04007788 \\ -0.04029503 & -0.04029503 & 0.07131029 \end{pmatrix} \quad (\text{A12})$$

$$\mathbf{K}_{1,-1,2} = \mathbf{K}_{-1,1,-2} = \begin{pmatrix} -0.003171257 & -0.03711247 & 0.04007788 \\ -0.03711209 & -0.003171455 & -0.04007788 \\ 0.04029503 & -0.04029528 & 0.07131029 \end{pmatrix} \quad (\text{A13})$$

$$\mathbf{K}_{1,-1,-2} = \mathbf{K}_{-1,1,2} = \begin{pmatrix} -0.003171257 & -0.03711247 & -0.04007829 \\ -0.03711209 & -0.003171455 & 0.04007829 \\ -0.04029503 & 0.04029528 & 0.0713109 \end{pmatrix} \quad (\text{A14})$$

$$\mathbf{K}_{-1,-2,1} = \mathbf{K}_{1,2,-1} = \begin{pmatrix} -0.003171455 & 0.04007829 & -0.03711209 \\ 0.04029528 & 0.0713109 & -0.04029503 \\ -0.03711247 & -0.04007829 & -0.003171257 \end{pmatrix} \quad (\text{A15})$$

$$\mathbf{K}_{-1,-2,-1} = \mathbf{K}_{1,2,1} = \begin{pmatrix} -0.003171455 & 0.04007829 & 0.03711247 \\ 0.04029528 & 0.0713109 & 0.04029528 \\ 0.03711247 & 0.04007829 & -0.003171455 \end{pmatrix} \quad (\text{A16})$$

$$\mathbf{K}_{1,-2,-1} = \mathbf{K}_{-1,2,1} = \begin{pmatrix} -0.003171257 & -0.04007829 & -0.03711247 \\ -0.04029503 & 0.0713109 & 0.04029528 \\ -0.03711209 & 0.04007829 & -0.003171455 \end{pmatrix} \quad (\text{A17})$$

$$\mathbf{K}_{1,-2,1} = \mathbf{K}_{-1,2,-1} = \begin{pmatrix} -0.003171257 & -0.04007829 & 0.03711209 \\ -0.04029503 & 0.0713109 & -0.04029503 \\ 0.03711209 & -0.04007829 & -0.003171257 \end{pmatrix} \quad (\text{A18})$$

$$\mathbf{K}_{-2,-1,1} = \mathbf{K}_{2,1,-1} = \begin{pmatrix} 0.0713109 & 0.04029528 & -0.04029503 \\ 0.04007829 & -0.003171455 & -0.03711209 \\ -0.04007829 & -0.03711247 & -0.003171257 \end{pmatrix} \quad (\text{A19})$$

$$\mathbf{K}_{-2,-1,-1} = \mathbf{K}_{2,1,1} = \begin{pmatrix} 0.0713109 & 0.04029528 & 0.04029528 \\ 0.04007829 & -0.003171455 & 0.03711247 \\ 0.04007829 & 0.03711247 & -0.003171455 \end{pmatrix} \quad (\text{A20})$$

$$\mathbf{K}_{2,-1,-1} = \mathbf{K}_{-2,1,1} = \begin{pmatrix} 0.0713109 & -0.04029528 & -0.04029528 \\ -0.04007788 & -0.003171455 & 0.03711247 \\ -0.04007788 & 0.03711247 & -0.003171455 \end{pmatrix} \quad (\text{A21})$$

$$\mathbf{K}_{2,-1,1} = \mathbf{K}_{-2,1,-1} = \begin{pmatrix} 0.07131029 & -0.04029528 & 0.04029503 \\ -0.04007788 & -0.003171455 & -0.03711209 \\ 0.04007788 & -0.03711247 & -0.003171257 \end{pmatrix} \quad (\text{A22})$$

ACKNOWLEDGEMENTS

We would like to gratefully acknowledge the support of the NSF, and also the NSF-IGERT program. We would also like to thank the NSF Summer Institute on Nano Mechanics and Materials for their support of this research.

REFERENCES

1. Haile JM. *Molecular Dynamics Simulations*. Wiley: New York, 1992.
2. Allen MP, Tildesley DJ. *Computer Simulation of Liquids*. Oxford University Press: Oxford, 1987.
3. Hughes TJR. *The Finite Element Method: Linear Static and Dynamic Finite Element Analysis*. Prentice-Hall: Englewood Cliffs, NJ, 1987.
4. Belytschko T, Liu WK, Moran B. *Nonlinear Finite Elements for Continua and Structures*. Wiley: New York, 2002.
5. Adelman SA, Doll JD. Generalized Langevin equation approach for atom/solid-surface scattering: general formulation for classical scattering off harmonic solids. *Journal of Chemical Physics* 1976; **64**:2375–2388.
6. Cai W, DeKoning M, Bulatov VV, Yip S. Minimizing boundary reflections in coupled-domain simulations. *Physical Review Letters* 2000; **85**:3213–3216.
7. Weinan E, Huang ZY. A dynamic atomistic-continuum method for the simulation of crystalline materials. *Journal of Computational Physics* 2002; **182**:234–261.
8. Wagner GJ, Karpov EG, Liu WK. Molecular dynamics boundary conditions for regular crystal lattices. *Computer Methods in Applied Mechanics and Engineering* 2004; **193**:1579–1601.
9. Karpov EG, Wagner GJ, Liu WK. A Green's function approach to deriving wave-transmitting boundary conditions in molecular dynamics simulations. *International Journal for Numerical Methods in Engineering* 2005; **62**:1250–1262.
10. Karpov EG, Stephen NG, Liu WK. Initial tension in randomly disordered periodic lattices. *International Journal of Solids and Structures* 2003; **40**(20):5371–5388.
11. Daw MS, Baskes ML. Embedded-atom method: derivation and application to impurities, surfaces, and other defects in metals. *Physical Review B* 1984; **29**(12):6443–6453.
12. Holian BL, Voter AF, Wagner NJ, Ravelo RJ, Chen SP, Hoover WG, Hoover CG, Hammerberg JE, Dontje TD. Effects of pairwise versus many-body forces on high-stress plastic deformation. *Physical Review A* 1991; **43**(6):2655–2661.
13. Kadowaki H, Liu WK. Bridging multi-scale method for localization problems. *Computer Methods in Applied Mechanics and Engineering* 2004; **193**:3267–3302.
14. Wagner GJ, Liu WK. Coupling of atomistic and continuum simulations using a bridging scale decomposition. *Journal of Computational Physics* 2003; **190**:249–274.
15. Park HS, Liu WK. Introduction and tutorial on multiple scale analysis in solids. *Computer Methods in Applied Mechanics and Engineering* 2004; **193**:1733–1772.
16. Park HS, Karpov EG, Klein PA, Liu WK. The bridging scale for two-dimensional atomistic/continuum coupling. *Philosophical Magazine* 2005; **85**(1):79–113.

17. Park HS, Karpov EG, Liu WK. A temperature equation for coupled atomistic/continuum simulations. *Computer Methods in Applied Mechanics and Engineering* 2004; **193**:1713–1732.
18. Xiao SP, Belytschko T. A bridging domain method for coupling continua with molecular dynamics. *Computer Methods in Applied Mechanics and Engineering* 2004; **193**:1645–1669.
19. Karpov EG, Park HS, Liu WK, Dorofeev DL. On the modeling of chaotic thermal motion in solids, Preprint.
20. Weeks TW. Numerical inversion of Laplace transforms using Laguerre functions. *Journal of the ACM* 1966; **13**:419–429.
21. Belytschko T, Lu YY, Gu L. Element-free Galerkin methods. *International Journal for Numerical Methods in Engineering* 1994; **37**:229–256.
22. Liu WK, Jun S, Zhang YF. Reproducing kernel particle methods. *International Journal for Numerical Methods in Fluids* 1995; **20**:1081–1106.
23. Park HS, Karpov EG, Klein PA, Liu WK. Three-dimensional bridging scale analysis of dynamic fracture. *Journal of Computational Physics* 2005, in press.
24. Foiles SM, Baskes ML, Daw MS. Embedded-atom-method functions for the fcc metals Cu, Ag, Au, Ni, Pd, Pt, and their alloys. *Physical Review B* 1986; **33**(12):7893–7991.
25. Tahoe. <http://tahoe.ca.sandia.gov>.